

Searching for molecular outflows in hyperluminous infrared galaxies

D. Calderón,¹★ F. E. Bauer,^{1,2,3} S. Veilleux,^{4,5} J. Graciá-Carpio,⁶ E. Sturm,⁶ P. Lira,⁷
S. Schulze^{1,2} and S. Kim¹

¹*Instituto de Astrofísica, Facultad de Física, Pontificia Universidad Católica de Chile, 782-0436 Santiago, Chile*

²*Millennium Institute of Astrophysics, Santiago, Chile*

³*Space Science Institute, 4750 Walnut Street, Suite 205, Boulder, Colorado 80301, USA*

⁴*Department of Astronomy, University of Maryland, College Park, MD 20742, USA*

⁵*Joint Space-Science Institute, University of Maryland, College Park, MD 20742, USA*

⁶*Max-Planck-Institut für extraterrestrische Physik, Postfach 1312, D-85741 Garching, Germany*

⁷*Departamento de Astronomía, Universidad de Chile, Casilla 36-D, Santiago, Chile*

Accepted 2016 May 18. Received 2016 May 17; in original form 2015 October 8

ABSTRACT

We present constraints on the molecular outflows in a sample of five hyperluminous infrared galaxies using *Herschel* observations of the OH doublet at 119 μm . We have detected the OH doublet in three cases: one purely in emission and two purely in absorption. The observed emission profile has a significant blueshifted wing suggesting the possibility of tracing an outflow. Out of the two absorption profiles, one seems to be consistent with the systemic velocity while the other clearly indicates the presence of a molecular outflow whose maximum velocity is about $\sim 1500 \text{ km s}^{-1}$. Our analysis shows that this system is in general agreement with previous results on ultraluminous infrared galaxies and QSOs, whose outflow velocities do not seem to correlate with stellar masses or starburst luminosities (star formation rates). Instead, the galaxy outflow likely arises from an embedded active galactic nuclei.

Key words: ISM: jets and outflows – ISM: molecules – galaxies: active – galaxies: evolution – quasars: general.

1 INTRODUCTION

Many hierarchical growth scenarios for galaxies have invoked co-evolution and symbiotic feedback between galaxies and their central supermassive black holes (SMBHs; e.g. Merloni, Rudnick & Di Matteo 2004; Bower et al. 2006) in order to explain (1) the tight relation between host galaxy spheroid and SMBH masses (Ferrarese & Merritt 2000; Gebhardt et al. 2000; Ferrarese et al. 2006; Côté et al. 2009), (2) the stark contrast between predicted and observed galaxy luminosity functions (Benson et al. 2003), and (3) the crude similarity between the global star formation and SMBH accretion rate histories over cosmic time (Madau & Dickinson 2014). In particular, it is now believed that strong feedback from active galactic nuclei (AGN) plays a significant role in galaxy evolution, abruptly quenching star formation to produce the ‘red and dead’ massive galaxies that we see today (Benson et al. 2003; Di Matteo, Springel & Hernquist 2005; Bower et al. 2006; Croton et al. 2006), and polluting the intergalactic and intracluster media with metals (e.g. Gaspari, Ruszkowski & Sharma 2012). Evidence for such feedback has been steadily growing over the years (e.g. Veilleux, Cecil & Bland-Hawthorn 2005; Fabian 2012; González-Alfonso et al. 2014). For instance, detections of moderate-to-high velocity ion-

ized outflows ($100\text{--}1000 \text{ km s}^{-1}$) have now been reported both as spatially resolved and kinematically distinct emission lines from ionization regions or in absorption along the line of sight towards numerous QSOs and Seyfert galaxies (e.g. Reeves, O’Brien & Ward 2003; Chartas et al. 2007, 2009; Krongold et al. 2007; Kraemer et al. 2009; Reeves et al. 2014). These studies have directly shown that AGN can produce such feedback, and even hinted that the degree of feedback may scale with SMBH mass and accretion power. None the less, many questions still remain about the underlying physics by which AGN-driven energy and momentum might be transferred to the interstellar medium (ISM) and molecular clouds ultimately responsible for star formation.

A number of recent studies have provided observational evidence that neutral and molecular gas outflows also appear to be common in both AGN and ultraluminous infrared galaxies (hereafter ULIRGs). Rupke, Veilleux & Sanders (2005) was among the first to spatially resolve and map the outflow within the closest powerful ULIRG Mrk 231. Rupke & Veilleux (2011) later detected strongly blueshifted ($\sim 1000 \text{ km s}^{-1}$) optical Na I D $\lambda\lambda 5890, 5896$ in absorption at $\sim 2 \text{ kpc}$ from Mrk 231’s nucleus, and Rupke & Veilleux (2013) used Keck/OSIRIS adaptive optics observations to improve the spatial resolution of Mrk 231’s previously observed outflow by a factor > 10 , measuring a terminal velocity of $\gtrsim 1300 \text{ km s}^{-1}$. Concurrently, Fischer et al. (2010) discovered a $\sim 1000 \text{ km s}^{-1}$ molecular outflow in Mrk 231 as traced by *Herschel* far-infrared

*E-mail: dcaldero@astro.puc.cl

(FIR) observations of OH in absorption, while Feruglio et al. (2010) detected spatially resolved CO emission in an $\sim 700 \text{ km s}^{-1}$ outflow using the IRAM/PdB Interferometer. Remarkably, the outflow mass rate estimated from OH and CO observations were in agreement within uncertainties (in the range $700\text{--}1000 M_{\odot} \text{ yr}^{-1}$). This estimate is significantly larger than the star formation rate (hereafter SFR) of $\sim 140 M_{\odot} \text{ yr}^{-1}$ found in the host galaxy (Veilleux et al. 2009). Based on the energy requirements and the fact that the outflows appear to arise largely from the nucleus and not from nearby star-forming regions, an AGN origin is generally favoured in Mrk 231.

More generally, Sturm et al. (2011) reported the detection of massive molecular outflows traced by OH in several additional ULIRGs, suggesting that the AGN luminosity and the AGN contribution to the total infrared (IR) luminosity seem to be correlated with the outflow terminal velocities and anticorrelated with the gas depletion time-scales. It is important to remark that OH lines are often associated with molecular H_2 clouds that are somewhat perturbed from equilibrium. More recently, Veilleux et al. (2013, hereafter V13) presented a detailed study of a sample of 43 ULIRGs and QSOs at $z \sim 0.3$ which were observed with *Herschel* using the OH doublet at $119 \mu\text{m}$ to characterize their molecular outflows. V13 found that the molecular outflows in these systems do not show any obvious dependence on SFR, although they warn that the range of SFRs probed by their sample is relatively narrow (~ 1 dex). Furthermore, V13 found that ULIRGs with large AGN fractions and luminosities show OH features that are more blueshifted, particularly for objects with $\log(L_{\text{AGN}}/L_{\odot}) \geq 11.8 \pm 0.3$. Finally, Spoon et al. (2013) found that 15 out of 24 ULIRGs with $z < 0.262$ showed evidence for molecular outflows in the 79 and $119 \mu\text{m}$ OH doublets, with velocities $> 700 \text{ km s}^{-1}$, implying that AGN were likely necessary to power these high-speed outflows. Notably, none of these works included the most powerful luminous IR galaxies, so-called hyperluminous infrared galaxies (hereafter HLIRGs). HLIRGs are beacons pinpointing the extremes of both star formation and perhaps AGN accretion, and thus could provide clues about how the processes at work might scale with AGN power and SFR. Furthermore, while such systems relatively rare at low redshift, ULIRGs and HLIRGs are perhaps 100 times more common at high- z (Casey, Narayanan & Cooray 2014; Assef et al. 2015; Tsai et al. 2015), potentially providing more relevant contributions to the star formation and accretion densities at these epochs (e.g. Magnelli et al. 2011, 2013; Buchner et al. 2015) and serving as the likely progenitors for modern-day massive elliptical galaxies (e.g. Sanders et al. 1988).

In this work, we analyse, for the first time, a sample of five HLIRGs in order to constrain their molecular outflows. We observed the rest-frame $118\text{--}121 \mu\text{m}$ spectral region for each of

these HLIRGs with *Herschel* to detect the molecular OH doublet at $119 \mu\text{m}$ in emission or absorption and measure its outflow velocity. We found that three out of five HLIRGs present the OH doublet feature and only one of them shows unambiguous signatures consistent with a molecular outflow. In Section 2, we describe the galaxy sample. In Section 3, we outline the reduction and analysis of the observations. We present the results of this study in Section 4 and interpreted them in Section 5. Finally, we summarize our conclusions in Section 6. In this work, we adopt $H_0 = 70 \text{ km s}^{-1} \text{ Mpc}^{-1}$, $\Omega_M = 0.3$, and $\Omega_{\Lambda} = 0.7$. We also adopt the standard convention that approaching material has a negative velocity with respect to the systemic velocity of the host galaxy due to Doppler shift.

2 SAMPLE

2.1 Sample selection

Our sample was selected from a parent sample studied by Ruiz, Carrera & Panessa (2007) which contains 14 HLIRGs. From this sample, we took four relatively local galaxies ($z < 0.5$) with very high IR luminosities ($\gtrsim 10^{13} L_{\odot}$) to build a subsample of very bright sources ($S_{100 \mu\text{m}} > 0.7 \text{ Jy}$) in order to perform high signal-to-noise (S/N) ratio *Herschel* observations in a reasonable amount of observational time. All galaxies in the sample are late-stage mergers with several lines of evidence indicating that these objects host powerful AGN. Furthermore, we added another galaxy previously observed with *Herschel* and that satisfies the same selection criteria (see Section 3).

Previously measured galaxy properties are summarized in Table 1. We initially adopted redshift measurements from the literature, but found that some published values lacked associated errors and were considered less reliable. To remedy this, we obtained redshifts from new spectroscopic observations for two galaxies in our sample, which we adopt below and provide in Table 1; reduction details are presented in Appendix A.

2.2 AGN fraction and stellar masses

We proceed to characterize the AGN power of the galaxies in our sample, based on the estimated galaxy properties from the previous subsection. First, we calculated the bolometric luminosity L_{bol} of the galaxies between 8 and $1000 \mu\text{m}$, the so-called IR luminosity L_{IR} (Sanders & Mirabel 1996), which are listed in Table 1. To accomplish this, we used the expression $L_{\text{bol}} = 1.15 L_{\text{IR}}$ from Veilleux et al. (2009), based on the average value for local ULIRGs (Kim & Sanders 1998). Then, we calculated the so-called AGN fraction, which is the fractional contribution of the AGN to the total

Table 1. Galaxy properties.

IRAS name (1)	Type (2)	z (3)	$\log\left(\frac{L_{\text{IR}}}{L_{\odot}}\right)$ (4)	$S_{100 \mu\text{m}}$ (Jy) (5)	$\log\left(\frac{L_X}{L_{\odot}}\right)$ (6)	t_{exp} (h) (7)	OBS-ID (8)
F00183–7111*	AGN2	0.3282 ± 0.0005	13.13	1.19	11.6	6.7	1342245966
00397–1312	AGN2	0.2617 ± 0.0001	12.90	1.90	–	4.9	1342238350
07380–2342	AGN2	0.2924 ± 0.0002	13.49	3.55	< 9.0	0.8	1342245974
12514+1027*	AGN2	0.3192 ± 0.0003	12.92	0.76	10.0	11.8	1342248537, 1342248539
14026+4341	QSO1	0.3243 ± 0.0003	13.11	0.99	< 9.3	9.6	1342257687, 1342257688

Notes. Column 1: IRAS galaxy names. Column 2: AGN type from Ruiz et al. (2007). Column 3: redshifts from Saunders et al. (2000), except for the objects marked with an asterisk for which we used our own estimated values (see Appendix A). Column 4: IR luminosity L_{IR} , spanning $8\text{--}1000 \mu\text{m}$ Ruiz et al. (2007). Column 5: flux density at $100 \mu\text{m}$ from Ruiz et al. (2007). Column 6: X-ray luminosity L_X spanning $0.2\text{--}10 \text{ keV}$ from Ruiz et al. (2007). Column 7: total PACS exposure time of our observations, except for IRAS 00397–1312 which was previously observed as part of programme *OT1_dfarrah_1*. Column 8: *Herschel* observation ID.

Table 2. Estimated galaxy properties.

IRAS name (1)	f_{15}/f_{30} (2)	α_{AGN} (per cent) (3)	$\log(L_{\text{bol}}/L_{\odot})$ (4)	$\log(L_{\text{bol}}^{\text{AGN}}/L_{\odot})$ (5)	$\log(L_{\text{bol}}^{\text{SB}}/L_{\odot})$ (6)	$\text{Si}_{9.7\mu\text{m}}$ (7)
F00183–7111	0.117	52	13.19	12.91	12.87	-1.13 ± 0.02
00397–1312	0.152	63	12.96	12.76	12.53	-1.09 ± 0.03
07380–2342	0.855	99	13.55	13.54	11.66	-0.08 ± 0.01
12514+1027	0.270	80	12.98	12.89	12.27	-0.61 ± 0.02
14026+4341	0.420	90	13.17	13.12	12.19	-0.09 ± 0.01

Notes. Column 1: IRAS galaxy name. Column 2: 15–30 μm flux ratio estimated from the *Spitzer* spectra. Column 3: Percentage AGN contribution to the bolometric luminosity based on the f_{15}/f_{30} method. Column 4: bolometric luminosity obtained from the IR luminosity following Veilleux et al. (2009). Column 5: AGN bolometric luminosity obtained from the total bolometric luminosity and the AGN fraction. Column 6: starburst bolometric luminosity obtained from the total bolometric luminosity and the AGN fraction. Column 7: depth of the silicate absorption feature at 9.7 μm estimated following Stierwalt et al. (2013) using the *Spitzer* spectral data.

bolometric luminosity, i.e.

$$L_{\text{bol}} = L_{\text{AGN}} + L_{\text{SB}}, \quad (1)$$

$$= \alpha_{\text{AGN}} L_{\text{bol}} + L_{\text{SB}}, \quad (2)$$

where L_{AGN} and L_{SB} are the AGN and starburst contributions to the total luminosity of a given galaxy, respectively. Veilleux et al. (2009) showed that the rest-frame 15–30 μm continuum ratio was correlated with the polycyclic aromatic hydrocarbon-free, silicate-free mid-IR (MIR)/FIR ratio and the AGN contribution to the bolometric luminosity more than any other *Spitzer*-derived continuum ratio they explored; we adopt the prescription based on this finding, which is referred as *Method #6* in their work. Basically, it consists in adopting $\log(f_{30}/f_{15}) = 0$ and 1.35 as zero-points for pure AGN and pure starburst ULIRGs, respectively (entries in table 9 from Veilleux et al. 2009). Then, using the bolometric corrections from table 10 and the formula given in the notes of table 11, both from Veilleux et al. (2009); we obtain the bolometric α_{AGN} . To apply this procedure, we make use of *Spitzer* spectra in the range $\sim 4\text{--}40$ μm of the galaxies in our sample, which we obtained from the IRS Enhanced Products catalogue. As none of the rest-frame spectra sampled the continuum at 30 μm (except for IRAS 00397–1312), we linearly extrapolated the data we had to estimate a value of the continuum at this wavelength. The absolute uncertainty on α_{AGN} values is about ± 20 per cent on average. With this estimate and the bolometric luminosity, we can compute L_{AGN} and L_{SB} using equations (1) and (2). Furthermore, we measured the depth of the silicate feature at 9.7 μm , $\text{Si}_{9.7\mu\text{m}}$ (Stierwalt et al. 2013). This quantity is a measure of the obscuration in ULIRGs. This depth is estimated as the logarithm of the ratio of the measured flux at 9.7 μm relative to the local continuum (i.e. more negative values indicate stronger absorption features). The results of this analysis are shown in Table 2.

Finally, we made use of photometric measurements as tracers of the stellar mass content in the galaxies. We used *Hubble Space Telescope* (*HST*) images obtained from the Mikulski Archive data base¹ and extracted the central point source from each galaxy, in order to exclude the AGN contribution, before performing the photometry. To do so, we generated theoretical point spread functions (PSFs) using TINY TIM (Krist, Hook & Stoehr 2011) and then we subtracted them from the extended sources using GALFIT (Peng et al. 2002). Finally, we ran Source Extractor (Bertin & Arnouts 1996) on the residual images and estimated Vega magnitudes to make direct comparisons with results from V13. Unfortunately, we found *HST* imaging data for only four of the five galaxies in our sample: two with *H* band (*F160W*) and two with *I* band (*F814W*). To augment

these, we include *H*-band data for three sources from the 2MASS data archive, which were not PSF subtracted. The 2MASS magnitudes at least provide strict upper limits on the stellar mass. The errors in the *HST* photometry are ~ 0.5 mag, incorporating both the PSF subtraction and photometry errors. The results of this procedure are presented in Table 3.

3 OBSERVATIONS, DATA REDUCTION AND SPECTRAL ANALYSIS

3.1 Observations

The HLIRG observations were carried out with the Photodetecting Array Camera and Spectrometer (PACS; Poglitsch et al. 2010) installed on *Herschel* (Pilbratt et al. 2010). Four galaxies were observed as part of programme *OT2_fbauer_1*, while the fifth object (IRAS 00397–1312) of our sample was previously observed also with *Herschel*/PACS as part of programme *OT1_dfarrah_1*. We used PACS in the range scan spectroscopy mode with high sampling, centred on the redshifted OH 119 μm + ¹⁸OH 120 μm complex with a velocity range of ~ 4000 km s^{-1} (rest-frame 118–121 μm), which is needed to provide enough spectral coverage on both sides of the OH complex for reliable continuum assessment. The resolution for our targets was ~ 240 km s^{-1} , which allowed us to detect outflow velocities up to 1000–2000 km s^{-1} .

3.2 Data reduction

The reduction procedure was identical to the one performed in Sturm et al. (2011) and V13. A standard PACS reduction and calibration was applied using the pipeline *ipipe* from HIPE 6.0. The spectra were normalized to the telescope flux and then recalibrated with previous Neptune observations during *Herschel*'s performance verification phase. Although the sources were not point-source corrected, this fact would not change the spectral shape of the sources. In all that follows, we only use the central spatial pixel alone due to its better S/N. For two objects in the sample (12514+1027 and 14026+4341), we obtained two separate observations. Therefore, we co-added them after confirming that they were consistent with each other. To combine them, we averaged the two observations as both exposure times were basically the same. After doing so, we analysed only the combined spectra.

3.3 Spectral analysis

Our analysis is analogous to the one performed by V13 on their ULIRGs+QSOs sample, which we describe briefly. The reduced

¹ <https://archive.stsci.edu/>

Table 3. Galaxy photometric measurements.

IRAS name (1)	m_{F160W} (2)	m_{F814W} (3)	M_{F160W} (4)	M_{F814W} (5)
F00183–7111	15.92 ± 0.18^a	–	-24.81 ± 0.18^a	–
00397–1312	16.6 ± 0.5	–	-23.6 ± 0.5	–
07380–2342	14.70 ± 0.07^a	17.3 ± 0.5	-25.80 ± 0.07^a	-23.2 ± 0.5
12514+1027	15.21 ± 0.11^a	18.6 ± 0.5	-22.48 ± 0.11^a	-22.1 ± 0.5
14026+4341	>18.8	–	>-21.9	–

Notes. Column 1: IRAS galaxy names. Column 2: PSF-subtracted apparent magnitude in the *HST* *F160W* band. Column 3: PSF-subtracted apparent magnitude in the *HST* *F814W* band. Column 4: absolute magnitude in the *HST* *F160W* band. Column 5: absolute magnitude in the *HST* *F814W* band.
^a*H*-band magnitudes without performing PSF subtraction taken from the 2MASS data archive.

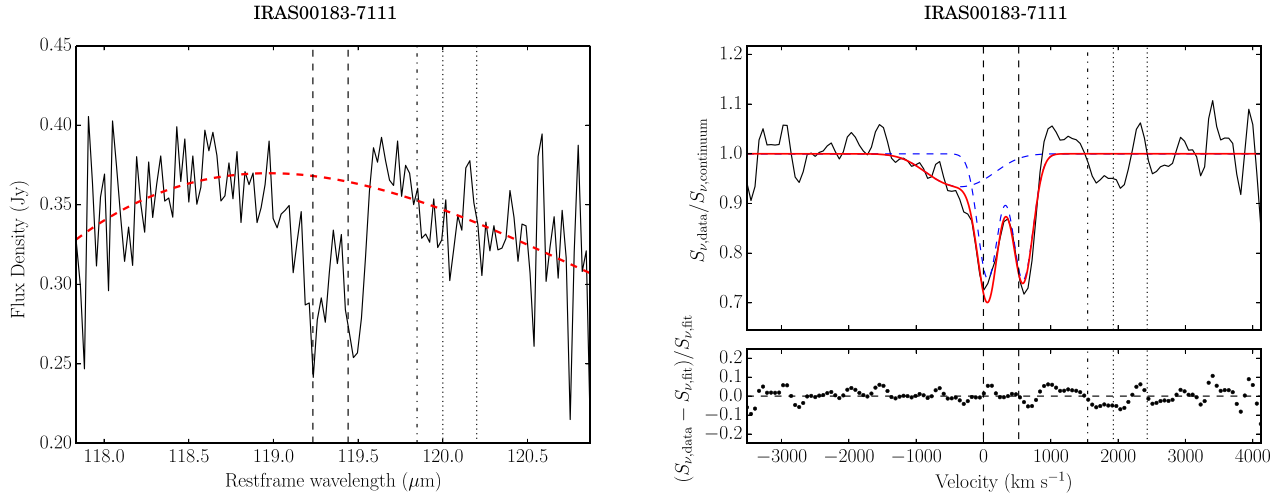


Figure 1. Spectral fits to the OH 119 μm doublet for the objects in our sample. On the left-hand panel, it is shown the reduced, not point-source corrected spectrum of IRAS F00183–7111 where the dashed red line represents the continuum fitted. On the right-hand panel, it is shown the smoothed spectrum divided by the continuum fit (solid black line) where the dashed blue lines are the velocity components of the doublet fit and the solid red line represents the total doublet fit (i.e. the sum of the components). The origin of the velocity in the x -axis corresponds to OH 119.233 μm at the systemic velocity. The two vertical dashed and dotted lines stand for the rest-frame location of the OH 119 μm and 120 μm doublets, respectively. The vertical dot–dashed line shows the position of the CH^+ 119.848 μm line. Furthermore, the lower box of the right-hand panel shows the residuals of the fit on the smoothed data.

Herschel spectra were smoothed using a Gaussian kernel with $\sigma = 0.025 \mu\text{m}$ to reduce the noise before analysing them. Then we fitted the base continuum level with a simple zero-order polynomial and divided the spectra by their continuum, in order to analyse the significance of the OH detection. When there was obvious curvature or a non-zero slope in the continuum component, we fitted a spline function instead. To characterize the OH 119.233, 119.441 μm doublet, we used two velocity components (a total of four Gaussians for the OH doublet). When the fit statistic for a single velocity component model was equal to or better than that of a two-velocity component model, we favoured the former. The least-square fits used the Levenberg–Marquardt algorithm to model the observed lines. Each Gaussian component is defined by its amplitude, peak position and standard deviation (full width at half-maximum). We kept fixed the separation of the lines to 0.208 μm in the rest frame ($\sim 520 \text{ km s}^{-1}$) and required that the amplitude and the standard deviation be fixed to the same value for each component in the doublet.

We analysed the OH doublet profile by measuring characteristic velocities from our fits, i.e. both velocity components fitted to the OH doublet; (1) $v_{50}(\text{abs})$, the median velocity of the fitted absorption profile, (2) $v_{84}(\text{abs})$, the velocity above which 84 per cent of the absorption takes place, (3) $v_{50}(\text{emi})$, the median velocity of the fitted emission profile, and $v_{84}(\text{emi})$, the velocity below which

84 per cent of the emission takes place. Also, we included the terminal outflow velocity, v_{max} , in our analysis, which is obtained from the maximum extent of the blueshifted wing of the 119.233 μm profile. The uncertainties on these characteristic velocities measurements are dominated by where we placed the continuum, and therefore we estimated errors by assuming different continuum shapes (spline or polynomial) and their positions. We found errors in v_{50} of $<100 \text{ km s}^{-1}$, in v_{84} of $\sim 100 \text{ km s}^{-1}$ and in v_{max} of $\sim 200 \text{ km s}^{-1}$.

4 RESULTS

The results of the OH 119 μm profile fits are shown in Figs 1–5, while the parameters derived from the spectral analysis are listed in Table 4. The OH doublet was detected in three out of five galaxies: in two galaxies (IRAS F00183–7111 and 12514+1027), the detections were purely in absorption, while in another (IRAS 00397–1312), it is purely in emission. For the two other objects (IRAS 07380–2342 and 14026+4341), we find that the spectra appear to be composed solely of continuum emission, and therefore the OH doublet may be either too weak or simply absent.

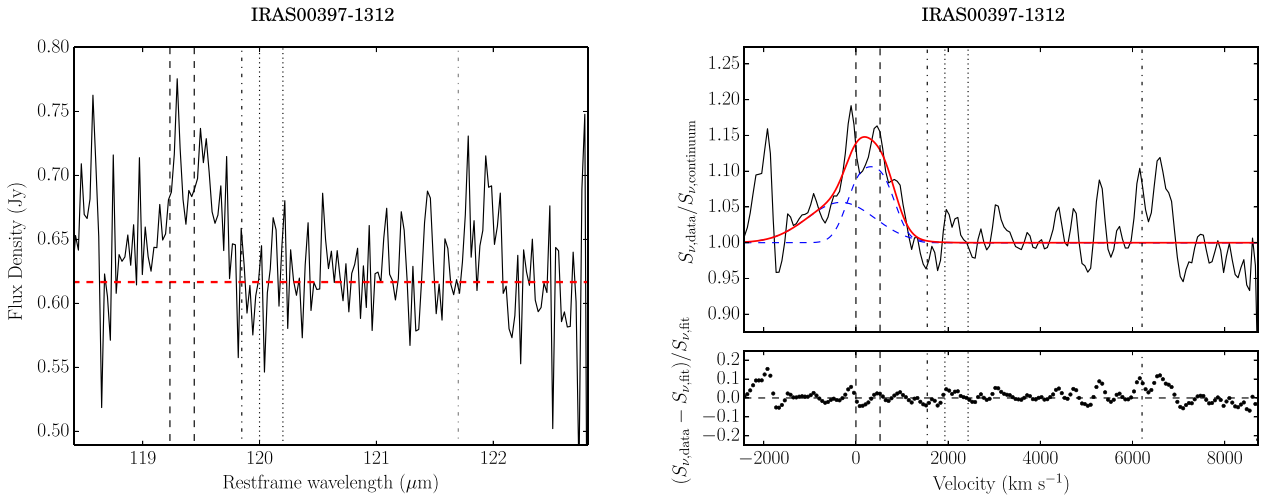


Figure 2. Analogous to Fig. 1 but for the galaxy IRAS 00397–1312. The vertical dot–dashed line here at $\lambda \sim 121.7 \mu\text{m}$ ($v \sim 6100 \text{ km s}^{-1}$) shows the position of the [N II] line.

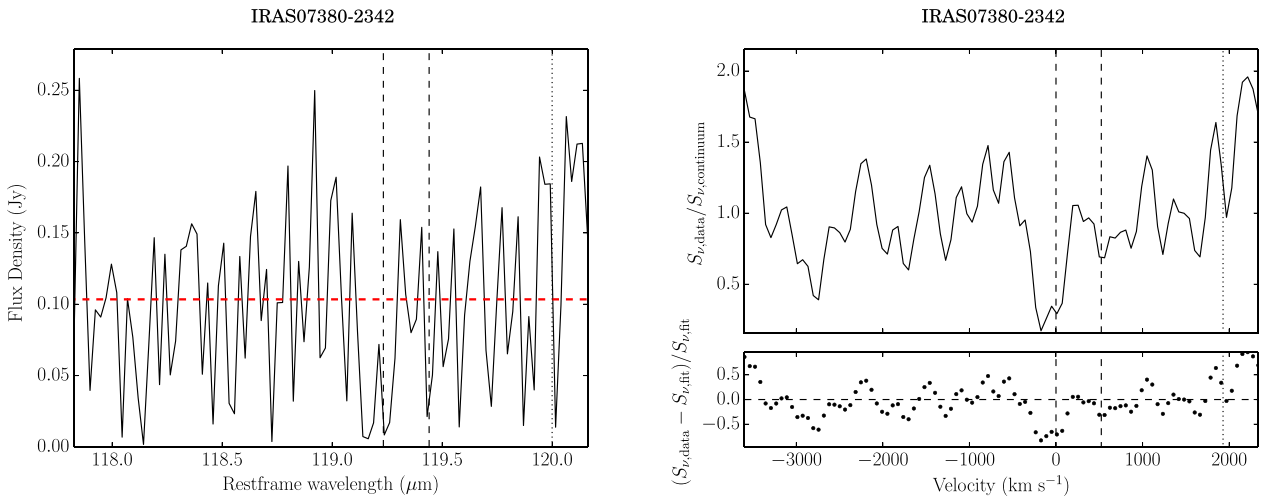


Figure 3. Analogous to Fig. 1 but for the galaxy IRAS 07380–2342.

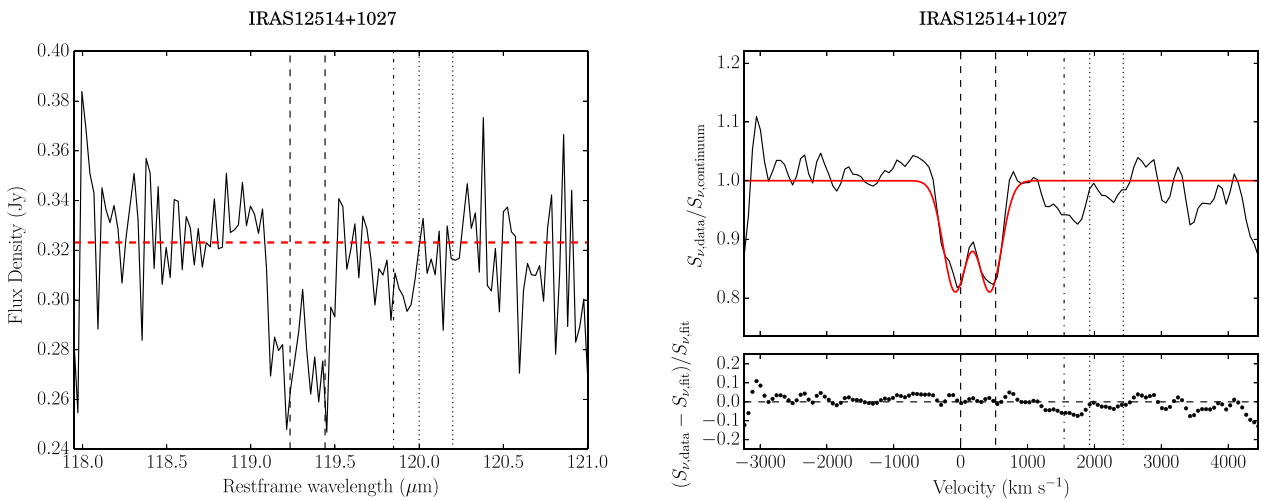


Figure 4. Analogous to Fig. 1 but for the galaxy IRAS 12514+1027.

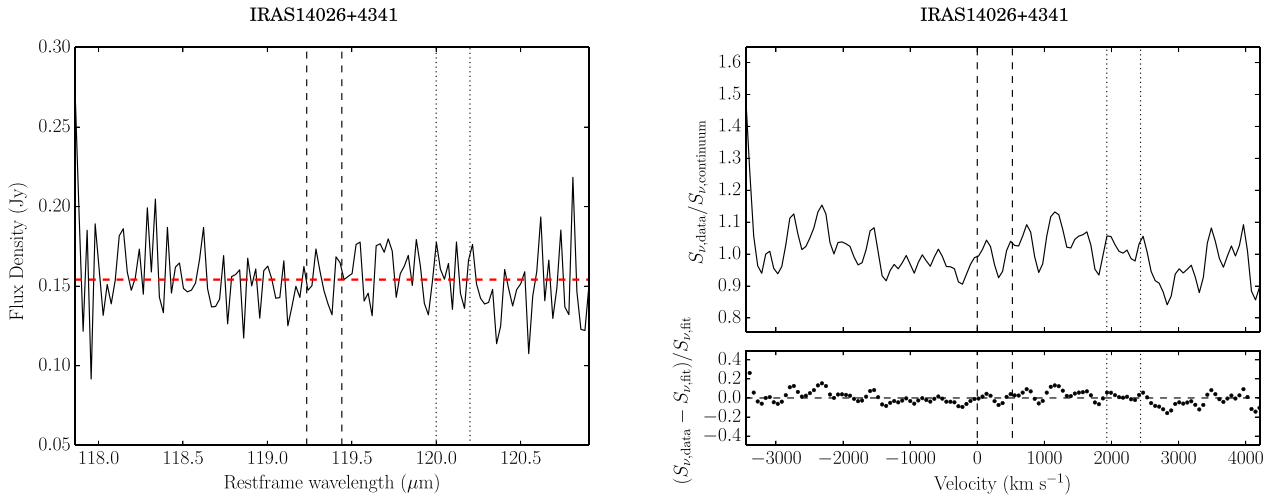


Figure 5. Analogous to Fig. 1 but for the galaxy IRAS 14026+4341.

Table 4. Spectral analysis measurements.

IRAS name (1)	$v_{50}(\text{abs})$ (2)	$v_{84}(\text{abs})$ (3)	$v_{\text{max}}(\text{abs})$ (4)	EW_{abs} (5)	$v_{50}(\text{emi})$ (6)	$v_{84}(\text{emi})$ (7)	EW_{emi} (8)
F00183–7111	70 ± 100	-470 ± 100	-1490 ± 300	130 ± 30	–	–	–
00397–1312	–	–	–	–	220 ± 60	590 ± 200	-100 ± 30
07380–2342	–	–	–	$<250^{\text{a}}$	–	–	$>-250^{\text{a}}$
12514+1027	-50 ± 60	-170 ± 60	-530 ± 200	90 ± 10	–	–	–
14026+4341	–	–	–	$<500^{\text{a}}$	–	–	$>-500^{\text{a}}$

Notes. Velocities and EWs are in units of km s^{-1} . Column 1: IRAS galaxy names. Column 2: median velocity of the absorption profile model fitted. Column 3: velocity above which 84 per cent of the absorption takes place. Column 4: maximum extent of the blueshifted wing of the absorption profile. Column 5: equivalent width for the absorption components. Column 6: median velocity of the emission profile model fitted. Column 7: velocity below which 84 per cent of the emission takes place. Column 8: equivalent width for the emission components.

^aThe limits appeared in absorption and emission, such that we can only constrain the absolute value of the EW in the spectra with no detection of the OH doublet.

4.1 Source by source analysis

4.1.1 IRAS F00183–7111

On the left-hand side panel of Fig. 1, we show the spectrum before analysing it. We can clearly see the OH doublet feature and probably a weak emission component. From the analysis, the best fit was reached by fitting a spline function to the continuum, which is denoted by a dashed red line. The right-hand panel shows the spectrum after being smoothed and divided by the fitted continuum. This allows us to distinguish that there is a significant blueshifted wing beyond the instrumental Gaussian tail of the strongest absorption component which we interpret as a molecular outflow with a $v_{\text{max}} \sim 1500 \text{ km s}^{-1}$.

4.1.2 IRAS 00397–1312

The spectrum is shown in Fig. 2 where we can recognize the OH doublet in emission and a weaker [NII]121.7 fine-structure line around $\lambda \sim 122 \mu\text{m}$. In this case, a better fit was found using a flat slope for the continuum. On the right-hand panel, we show the spectrum fitting the OH doublet with two doublets. A second doublet is needed to take into account the blueshifted wing that departs from the primary component. This feature may indicate the presence of an outflow, however, without an absorption component, we cannot be certain. Furthermore, a possible redshifted [N II] emission line may be present, although the S/N is too low to characterize it well.

4.1.3 IRAS 07380–2342

The spectrum of this galaxy is shown in the left-hand panel of Fig. 3. Although the doublet might be detected marginally in absorption, it is difficult to infer its presence with certainty due to the fact that the spectrum seems to be heavily dominated by the noise. This might be caused by a pointing offset when observing this galaxy, as the brightest pixel of the image is not at the centre.

4.1.4 IRAS 12514+1027

On the left-hand panel of Fig. 4, we see prominent absorption lines which correspond to the OH doublet and a weaker feature which could indicate the presence of the ^{18}OH 120 μm doublet. Although we only used a single-velocity component to fit the OH 119 μm doublet, it is possible that a bump at -1000 km s^{-1} is also part of the doublet, implying more complex velocity structure. However, as the main doublet is consistent with the systemic velocity of the galaxy, we cannot confirm a molecular outflow detection from this spectrum (see right-hand panel of Fig. 4).

4.1.5 IRAS 14026+4341

In this case, the spectrum appears only to be composed of continuum emission and is consistent with a flat model component (see Fig. 5).

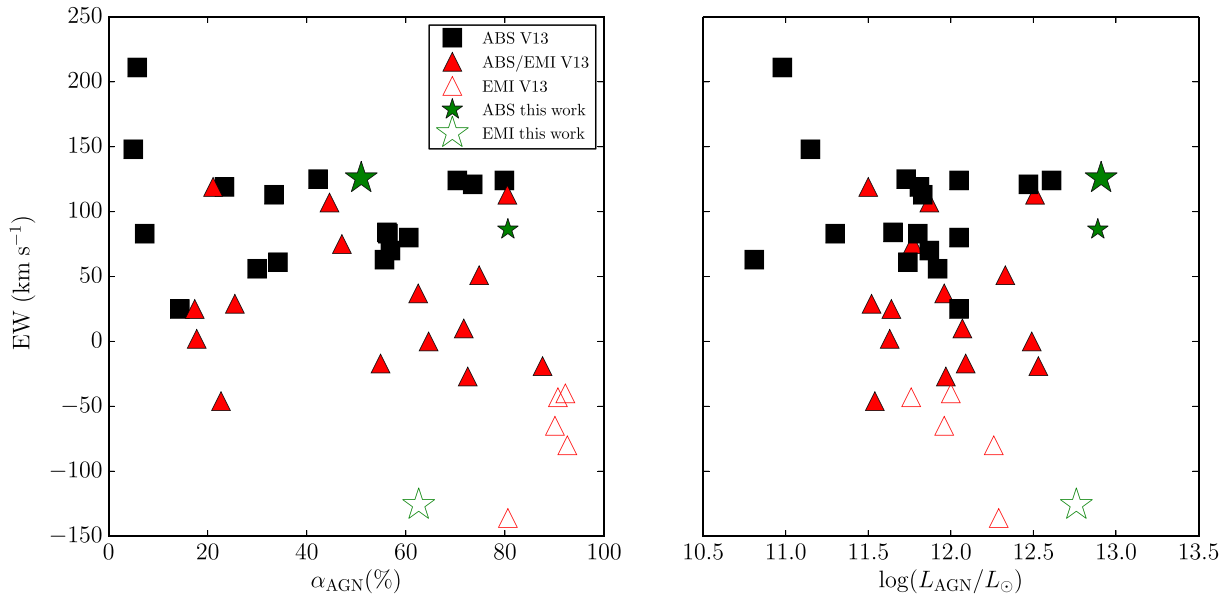


Figure 6. Total equivalent width of the $119\ \mu\text{m}$ doublet as a function of AGN fraction (left-hand panel) and AGN luminosity (right-hand panel). Black squares, filled red triangles, and open red triangles are ULIRGs from V13 with OH $119\ \mu\text{m}$ seen purely in absorption, composite absorption/emission, and purely in emission, respectively. Meanwhile, filled green and open green stars are HLIRGs from this work with the OH doublet seen purely in absorption and purely in emission.

5 DISCUSSION

We compared the spectral measurements with derived galaxy properties from Tables 2 and 3 to look for any signs of correlations. We included here the data from V13 (shown as black squares and red triangles), who performed an analogous procedure in a larger ULIRG sample. In this analysis, we included the three HLIRGs with OH detections, however, we have to keep in mind that only one source has signatures of having a molecular outflow. To highlight this fact, this galaxy is shown as a big green filled star in Figs 6–9.

Fig. 6 shows a general lack of correlation between the equivalent width of the OH feature and AGN fraction or AGN luminosity found by V13. Furthermore, we see our data points do not change this result. We have also studied the relation between the OH equivalent width and the obscuration of the systems using $\text{Si}_{9.7\ \mu\text{m}}$. This comparison is shown in Fig. 7, which plots the sources from V13 and this work data. The HLIRGs in our sample are not very obscured and do not have strong OH absorption, which, in principle, supports the correlation found by V13 that more obscured objects present a stronger OH absorption. Also, objects without OH detection (shown as black dashed lines) seem to support this idea.

In Fig. 8, we present the characteristic velocities measured from the absorption profiles of F00183–7111 and 12514+1027 as a function of H -band absolute magnitudes (left-hand panel) and starburst luminosities (right-hand panel). The results are largely consistent with those of V13 on ULIRGs and QSOs: there does not appear to be any strong relation between the molecular outflow velocities and the stellar masses of the hosts or the starburst luminosities (i.e. SFRs). We do note that v_{50} exhibits the smallest dispersion among the velocity measures, and there is a hint of an upward trend between v_{50} and SFR, which the addition of IRAS F00183–7111 appears to dramatically extend. However, it is important to stress that the V13 data do not cover a wide range of SFRs or stellar masses and, unfortunately, our new data do not extend these ranges either. Therefore, one should be cautious when interpreting the lack of obvious correlation between the velocities and SFRs or stellar masses.

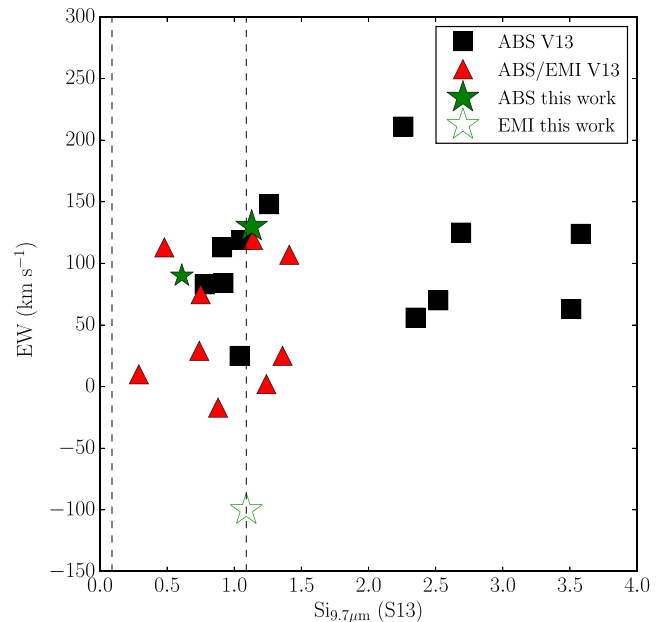


Figure 7. Equivalent width of the $119\ \mu\text{m}$ doublet as a function of the depth of the silicate feature at $9.7\ \mu\text{m}$ relative to the local continuum on a logarithmic scale measured by Stierwalt et al. (2013). The meaning of the symbols is the same as in Fig. 6. Vertical black dashed lines stand for the HLIRGs without OH detection.

In the left-hand panel of Fig. 9, we observe that the characteristic velocities of F00183–7111 roughly follow the same correlation with AGN fraction as found among ULIRGs, further suggesting that AGN activity plays a role in driving this outflow. When considering AGN luminosities: in the right-hand panel of Fig. 9, the outflow velocities of F00183–7111 seem to be consistent within the dispersion with the correlation between outflow velocity and AGN luminosity found by V13, except in the

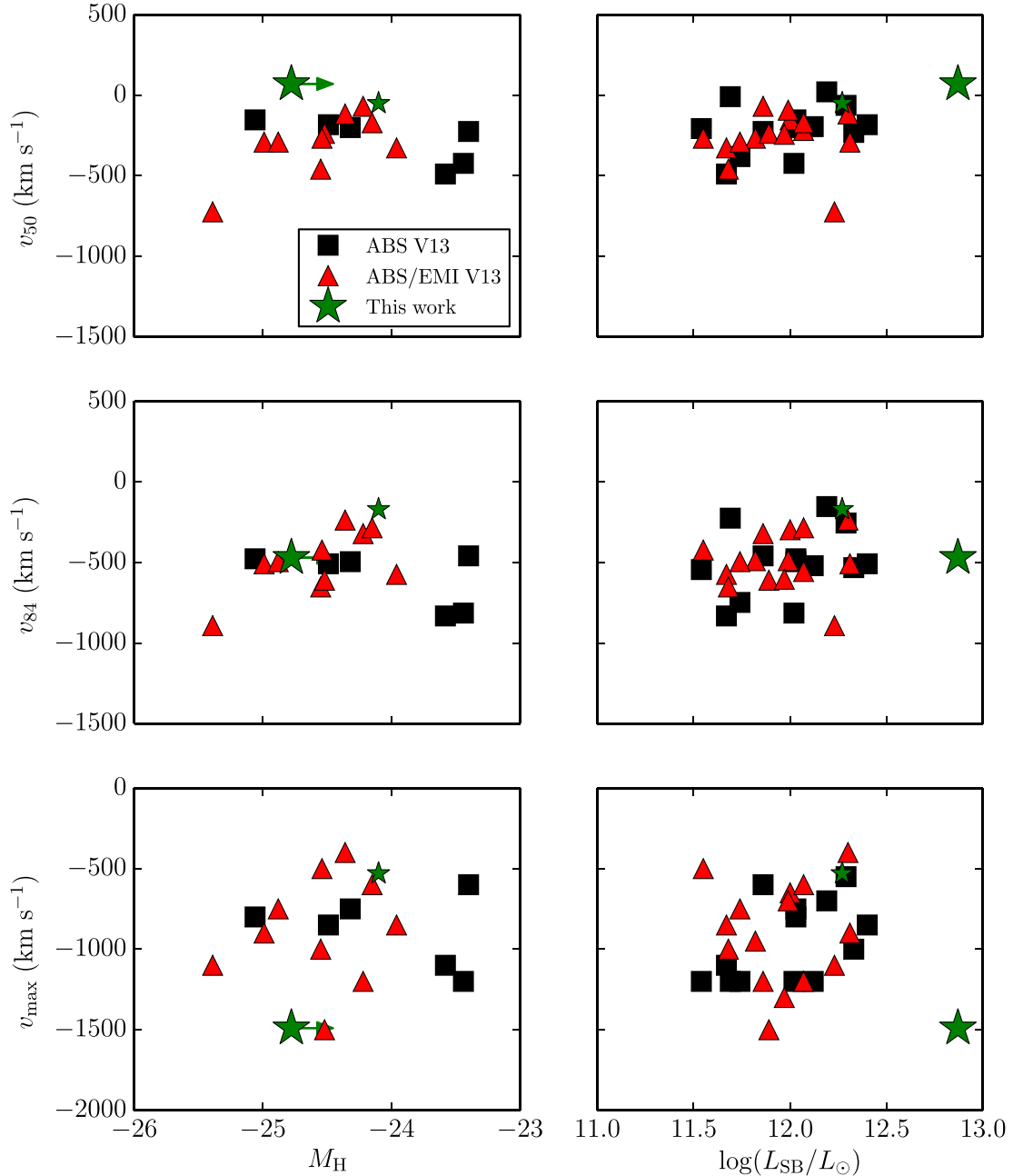


Figure 8. 50 per cent (upper), 84 per cent (central), and terminal (lower) OH outflow as a function of the absolute magnitude in H band on the left-hand panels, and starburst luminosity on the right-hand panels. The meaning of the symbols is the same as in Fig. 6.

case of v_{50} where F00183–7111 lies beyond the dispersion of the fit.

The fact that OH is observed in emission for IRAS 00397–1312 could indicate it is beginning to shed its dusty cocoon. However, α_{AGN} for the galaxy is only ~ 63 per cent, whereas the V13 objects seen with OH purely in emission all had $\alpha_{AGN} \gtrsim 80$ per cent, which is more consistent with the evolutionary scenario in which the AGN becomes more apparent once the merger remnant has cast off of its natal cocoon and the signatures of AGN feedback are predicted to wane (e.g. Narayanan et al. 2008; Hopkins, Murray & Thompson 2009).

Before jumping to conclusions, one has to remember that scatter in the measured outflow velocities is expected for several reasons:

(i) the measured outflow velocities may be underestimated due to projection effects, which depend on the exact geometry of each outflow; (ii) the kinematics of the outflowing material depend on several largely unconstrained variables (e.g. gas mass fraction and density, column density, dust content of individual cloudlets) associated with the complex multiphase nature of the entrained ISM and the exact acceleration mechanisms (e.g. radiation pressure, ram pressure, shocks); (Cooper et al. 2008) (iii) we are measuring time-averaged quantities which may not be exactly in phase: the AGN luminosity is derived from MIR measurements on kpc scales, while the outflow velocities are from FIR measurements on scales of a few hundreds of parsecs (corresponding to a few 10^6 yr for outflow speeds of a few hundred of km s $^{-1}$). Consequently, one cannot draw

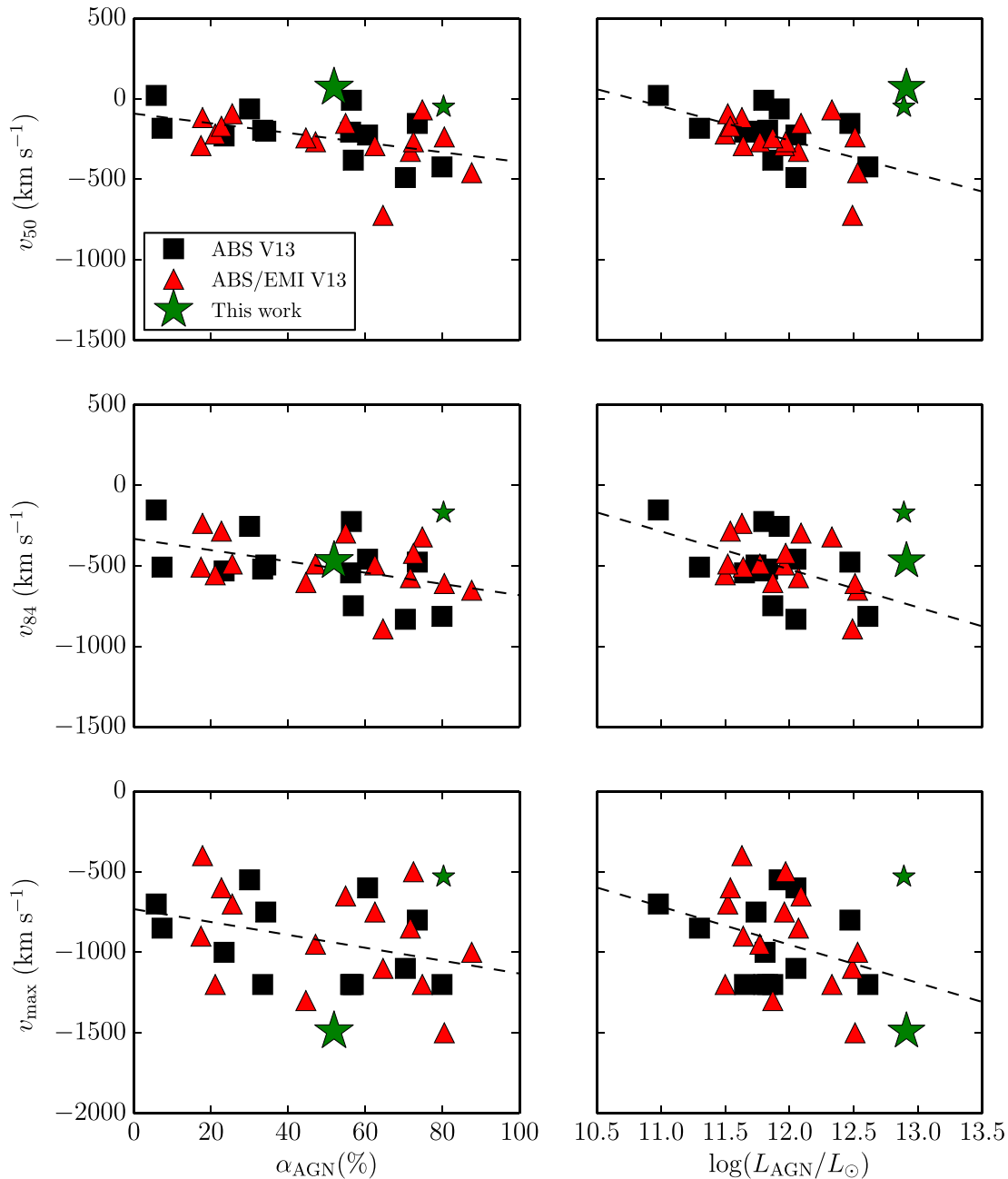


Figure 9. 50 per cent (upper), 84 per cent (central), and terminal (lower) OH outflow as a function of the AGN fractions on the left-hand panels, and AGN luminosity on the right-hand panels. The meaning of the symbols is the same as in Fig. 6.

any firm conclusions based on only two HLIRGs. A larger sample of HLIRGs will be needed for a more meaningful comparison with ULIRGs and QSOs.

6 CONCLUSIONS

We have analysed the *Herschel*/PACS spectrum of five HLIRGs, using the OH 119 μm doublet to search for molecular outflows. The OH doublet was detected in three out of five galaxies, from which one was purely in emission and two purely in absorption. Although it is possible that the OH detection in emission may indicate the presence of an outflow, the lack of a clear absorption component in the doublet does not allow us to conclude it with certainty. On the other hand, out of the two systems with OH detections in absorption,

only IRAS F00183–7111 seems to have a molecular outflow. The most blueshifted wing of its OH profile reached about 1500 km s^{-1} .

Our analysis supports the lack of correlation between the OH equivalent width and both AGN fraction and luminosity reported by V13. Furthermore, it agrees very well with the correlation between the OH equivalent width and the system obscuration also found by V13. The characteristic velocities of the outflow detected in IRAS F00183–7111 are in general agreement with previously studied correlations found in studies of local ULIRGs, specifically V13 and Spoon et al. (2013). This fact supports the idea that outflows are not related either to starburst activity or stellar mass. Instead, they support the notion that AGN are responsible for driving the powerful outflows seen in many ULIRGs/HLIRGs.

A larger sample of HLIRGs is clearly needed to explore these phenomena in more detail. We note that the *WISE* all-sky catalogue is already discovering large numbers of new HLIRGs (e.g. Eisenhardt et al. 2012; Tsai et al. 2013; Toba et al. 2015). Some fraction of these may lie at suitable redshifts whereby ground-based submillimeter facilities such as ALMA can probe any potential molecular outflows from them. Otherwise, progress may have to wait for a still to be defined future FIR space observatory.

ACKNOWLEDGEMENTS

We thank the anonymous referee for very useful comments and suggestion to improve this work. We acknowledge support from CONICYT-Chile grants, Basal-CATA PFB-06/2007 (DC, FEB, SS), FONDECYT 1141218 (FEB), PCCI 130074 (FEB), ALMA-CONICYT 31100004 (FEB), Gemini-CONICYT 32120003 (FEB), ‘EMBIGGEN’ Anillo ACT1101 (DC, FEB), the Ministry of Economy, Development, Tourism’s Millennium Science Initiative through grant IC120009 awarded to The Millennium Institute of Astrophysics, MAS (FEB, SS), CONICYT-Chile through PCHA/Doctorado Nacional (2015-21151574) (DC), and by NASA through Herschel contracts 1427277 and 1454738 (SV). Optical observations were obtained with the Magellan/Baade as part of the program CN–2015A–129. We acknowledge NASA and Mikulski Archive for Space Telescopes (MAST) for the use of data retrieved from MAST.

REFERENCES

- Assef R. J. et al., 2015, ApJ, 804, 27
 Benson A. J., Bower R. G., Frenk C. S., Lacey C. G., Baugh C. M., Cole S., 2003, ApJ, 599, 38
 Bertin E., Arnouts S., 1996, A&AS, 117, 393
 Bower R. G., Benson A. J., Malbon R., Helly J. C., Frenk C. S., Baugh C. M., Cole S., Lacey C. G., 2006, MNRAS, 370, 645
 Buchner J. et al., 2015, ApJ, 802, 89
 Casey C. M., Narayanan D., Cooray A., 2014, Phys. Rep., 541, 45
 Chartas G., Brandt W. N., Gallagher S. C., Proga D., 2007, AJ, 133, 1849
 Chartas G., Kochanek C. S., Dai X., Poindexter S., Garmire G., 2009, ApJ, 693, 174
 Cooper J. L., Bicknell G. V., Sutherland R. S., Bland-Hawthorn J., 2008, ApJ, 674, 157
 Côté P. et al., 2006, ApJ, 165, 57
 Croton D. J. et al., 2006, MNRAS, 365, 11
 Di Matteo T., Springel V., Hernquist L., 2005, Nature, 433, 604
 Eisenhardt P. R. M. et al., 2012, ApJ, 755, 173
 Fabian A. C., 2012, ARA&A, 50, 455
 Ferrarese L., Merritt D., 2000, ApJ, 539, L9
 Ferrarese L. et al., 2006, ApJ, 644, 21
 Feruglio C., Maiolino R., Piconcelli E., Menci N., Aussel H., Lamastra A., Fiore F., 2010, A&A, 518, L155
 Fischer J. et al., 2010, A&A, 518, L41
 Gaspari M., Ruzkowski M., Sharma P., 2012, ApJ, 746, 94
 Gebhardt K. et al., 2000, ApJ, 539, L13
 Genzel R. et al., 2014, ApJ, 796, 7
 González-Alfonso E. et al., 2014, A&A, 561, A27
 Hopkins P. F., Murray N., Thompson T. A., 2009, MNRAS, 398, 303
 Kim D.-C., Sanders D. B., 1998, ApJS, 119, 41
 Kraemer S. B., Trippe M. L., Crenshaw D. M., Meléndez M., Schmitt H. R., Fischer T. C., 2009, ApJ, 698, 106
 Krist J. E., Hook R. N., Stoehr F., 2011, in Kahan M. A., ed., Proc. SPIE Conf. Ser., Vol. 8127, Optical Modeling and Performance Predictions V. SPIE, Bellingham, p. 81270J-1
 Krongold Y., Nicastro F., Elvis M., Brickhouse N., Binette L., Mathur S., Jiménez-Bailón E., 2007, ApJ, 659, 1022
 Madau P., Dickinson M., 2014, ARA&A, 52, 415

- Magnelli B., Elbaz D., Chary R. R., Dickinson M., Le Borgne D., Frayer D. T., Willmer C. N. A., 2011, A&A, 528, A35
 Magnelli B. et al., 2013, A&A, 553, A132
 Merloni A., Rudnick G., Di Matteo T., 2004, MNRAS, 354, L37
 Narayanan D. et al., 2008, ApJS, 176, 331
 Peng C. Y., Ho L. C., Impey C. D., Rix H.-W., 2002, AJ, 124, 266
 Pilbratt G. L. et al., 2010, A&A, 518, L1
 Poglitsch A. et al., 2010, A&A, 518, L2
 Reeves J. N., O’Brien P. T., Ward M. J., 2003, ApJ, 593, 65
 Reeves J. N. et al., 2014, ApJ, 780, 45
 Ruiz A., Carrera F. J., Panessa F., 2007, A&A, 471, 775
 Rupke D. S. N., Veilleux S., 2011, ApJ, 729, L27
 Rupke D. S. N., Veilleux S., 2013, ApJ, 775, L15
 Rupke D. S., Veilleux S., Sanders D. B., 2005, ApJ, 632, 751
 Sanders D. B., Mirabel I. F., 1996, ARA&A, 34, 749
 Sanders D. B., Soifer B. T., Elias J. H., Madore B. F., Matthews K., Neugebauer G., Scoville N. Z., 1988, ApJ, 325, 74
 Saunders W. et al., 2000, MNRAS, 317, 55
 Spoon H. W. W. et al., 2013, ApJ, 7725, 127
 Stierwalt S. et al., 2013, ApJS, 206, 1
 Sturm E. et al., 2011, ApJ, 733, L16
 Toba Y. et al., 2015, PASJ, 67, 8615
 Tsai C.-W. et al., 2013, in Sun W.-H., Xu C. K., Scoville N. Z., Sanders D. B., eds, ASP Conf. Proc. Vol. 477, Galaxy Mergers in an Evolving Universe. Astron. Soc. Pac., San Francisco, p. 247
 Tsai C.-W. et al., 2015, ApJ, 805, 90
 Veilleux S., Cecil G., Bland-Hawthorn J., 2005, ARA&A, 43, 769
 Veilleux S. et al., 2009, ApJS, 182, 628
 Veilleux S. et al., 2013, ApJ, 776, 27 (V13)

APPENDIX A: REDSHIFT MEASUREMENTS

Given that systemic velocities are very important in the context of this work, we carried out spectroscopic observations for two galaxies in our sample: IRAS F00183–7111 and IRAS 12514+1027; in order to independently assess the accuracy of their redshifts. The spectra were measured using the Inamori Magellan Areal Camera Spectrograph (IMACS) on the Magellan I Baade 6.5 m telescope at Las Campanas Observatory. We obtained two exposures of 300 s for each object. The data reduction was performed using IRAF following standard procedures. The spectra presented prominent features in emission that allowed us to estimate its radial velocity easily (see Figs A1 and A2). To this end, we used the task *emsao* from the

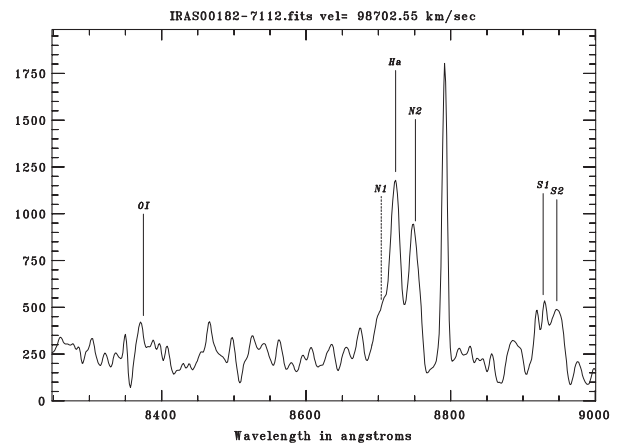


Figure A1. Smoothed IRAS F00183–7111 spectrum taken with Magellan/IMACS. The flux is in instrumental units. The line identification and radial velocity were performed with the task *emsao* from the *rvsao* package in IRAF.

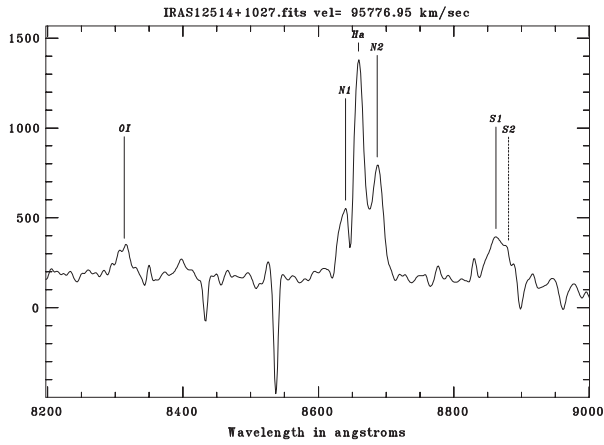


Figure A2. Analogous to Fig. A1 but for IRAS 12514+1027.

package *rvsao* to identify the redshifted emission lines and then to compute a radial velocity value. The measured redshifts and their associated errors are presented in Table 1. The errors account for the wavelength calibration solution, the aperture trace and the *emsao* algorithm uncertainties.

This paper has been typeset from a $\text{\TeX}/\text{\LaTeX}$ file prepared by the author.